REVIEW

Exploring sparsely populated states of macromolecules by diamagnetic and paramagnetic NMR relaxation

G. Marius Clore*

Laboratory of Chemical Physics, National Institute of Diabetes and Digestive and Kidney Diseases, National Institutes of Health, Bethesda, Maryland 20892-0520

Received 27 October 2010; Revised 2 December 2010; Accepted 3 December 2010
DOI: 10.1002/pro.576
Published online 17 December 2010 proteinscience.org

Abstract: Sparsely populated states of macromolecules, characterized by short lifetimes and high free-energies relative to the predominant ground state, often play a key role in many biological, chemical, and biophysical processes. In this review, we briefly summarize various new developments in NMR spectroscopy that permit these heretofore invisible, sparsely populated states to be detected, characterized, and in some instances visualized. Relaxation dispersion spectroscopy yields detailed kinetic information on processes involving species characterized by distinct chemical shifts with lifetimes in the ~50 μs–10 ms range and populations as low as 0.5%. In the fast exchange regime (time scale less than ~250–500 μs), the footprint of sparsely populated states can be observed on paramagnetic relaxation enhancement profiles measured on the resonances of the major species, thereby yielding structural information that is directly related to paramagnetic center-nuclei distances from which it is possible, under suitable circumstances, to compute a structure or ensemble of structures for the minor species. Finally, differential transverse relaxation measurements can be used to detect lifetime broadening effects that directly reflect the unidirectional rates for the conversion of NMR-visible into high-molecular weight NMR-invisible species. Examples of these various approaches are presented.

Keywords: high energy states; paramagnetic NMR; relaxation dispersion; paramagnetic relaxation enhancement; transient species

Many biological processes proceed via sparsely populated intermediates. These include, for example, the initial formation of encounter complexes in macromolecular association, target searching in specific protein-DNA recognition, conformational selection in ligand binding, conformational transitions associated with allostery, intermediates along the protein folding pathway, or in the course of enzyme catalysis, and early events in self-assembly processes. In general, the populations of these states at equilibrium are low and their lifetimes are short. Consequently, transient states arising from rare but rapid excursions between the global free energy minimum and higher free energy local minima are extremely challenging to

Grant sponsors: The intramural program of the NIDDK, NIH; The Intramural AIDS Targeted Antiviral Program of the Office of the Director of the NIH

*Correspondence to: Dr. G. Marius Clore, Laboratory of Chemical Physics, National Institute of Diabetes and Digestive and Kidney Diseases, National Institutes of Health, Bethesda, MD 20892-0520. E-mail: mariusc@intra.niddk.nih.gov.

study at atomic resolution under equilibrium conditions since they are effectively invisible to most structural and biophysical techniques including crystallography and conventional NMR spectroscopy. Recent developments in NMR, however, have rendered short-lived, sparsely populated states accessible to spectroscopic analysis, yielding considerable insights into their kinetics, thermodynamics, and structures.

Two main NMR methods have been developed over the last few years to probe rare states: relaxation dispersion (RD) spectroscopy and paramagnetic relaxation enhancement (PRE). RD spectroscopy is dependent on the existence of significant chemical shift differences between the NMR active nuclei (^{1}H, ^{15}N, or ^{13}C) in the various states, and in general can be used to probe events occurring on time scales ranging from about 50 μs−10 ms.[1–6] The PRE requires that the distances between a paramagnetic label and the monitored spins (usually protons) are significantly shorter in the sparsely populated state than in the major species, and that the lifetime of the minor species is less than ∼250−500 μs.[7–9] Most recently, a novel approach involving what might be termed differential transverse NMR relaxation has been used to study invisible species involving exchange on the millisecond time scale between an NMR-visible low molecular weight state (such as a monomer or low-order multimer) and NMR-invisible very high molecular weight forms such as fibrils, protofibrils or membrane-bound states.[10] Under suitable circumstances, all three techniques are capable of detecting states with populations as low as 0.5%. Since extensive and detailed reviews on RD spectroscopy[1–6] and the PRE[7–9] have been published, the current review will focus on a brief description of the salient points of the relevant theories and illustrate the application of these NMR techniques to various problems in biophysics and structural biology.

RD spectroscopy

In an exchanging system between multiple states, the transverse relaxation rate (R_2) is given by the sum of the intrinsic transverse relaxation rate R_2^0 and an exchange contribution R_{ex}.[1,11,12] The R_{ex} term is a function of the exchange rate k_{ex} (which in the case of a two-state exchange system is simply the sum of the forward and backward rate constants) and the chemical shift difference for the nucleus in the two distinct chemical environments. In the slow exchange regime, when k_{ex} is much (20-fold or more) smaller than the chemical shift difference (measured in radians s^{-1} given by 2π times the separation between the two resonance positions in units of Hz), two distinct resonances will be observed. In the fast exchange regime, when k_{ex} is much ($\geq$20) larger than the chemical shift difference, a single resonance will be observed at a position corresponding to the population weighted mean of the chemical shifts in the two states. In the extreme fast and slow exchange limits, the exchange contribution to the linewidth is negligible. In the intermediate regime, however, the R_{ex} term results in line broadening, which is most marked when k_{ex} is equal to the chemical shift difference. Under these conditions, even the presence of a state populated at the 0.5% level can cause significant line broadening of the resonances of the major species. The key to RD spectroscopy lies in the use of special pulse sequences to progressively attenuate the R_{ex} contribution to the measured R_2 rate.[11] This can be achieved by applying a train of refocusing pulses known as a Carr-Purcell-Meiboom-Gill sequence (CPMG)[13,14] while magnetization evolves under the influence of a chemical shift that varies stochastically as a result of the exchange process.[3] Because each nucleus follows a slightly different trajectory, dephasing of magnetization occurs resulting in larger R_{ex} rates and hence broader linewidths. By reducing the interval between the refocusing pulses (i.e., increasing the number of pulses during a fixed period T), dephasing is decreased, the R_{ex} term is reduced and the linewidths become narrower, and plots of the observed R_2 rate as a function of the interval between the refocusing pulses yields what is known as a RD curve with large observed R_2 rates at low CPMG repetition rates and small R_2 rates at high CPMG repetition rates. The detailed shape of the RD curve is a complex function of the exchange rate k_{ex}, the populations of the states, the chemical shift difference between the states and the CPMG repetition rate. For data recorded at a single magnetic field, the contribution of population and chemical shift difference to R_{ex} cannot be separated *a priori*. Thus, unless the population of the species or the chemical shift difference between these species is already known, deconvolution of these two terms necessitates recording RD data at different magnetic field strengths since the species populations are independent of magnetic field while the chemical shift difference in frequency units is linearly proportional to the magnetic field. Typically CPMG experiments can probe exchange processes with lifetimes ranging from ∼50 μs to ∼10 ms and occupancies for the minor species as low as 0.5−1%.[3] Similar RD data can also be obtained by measuring longitudinal R_1 relaxation rates in the rotating frame, known as $R_{1\rho}$, by varying the field strength of the applied spin-lock pulse.[12] Under suitable conditions $R_{1\rho}$ RD can probe lifetimes potentially as short as ∼5 μs.

Information content of RD data

The key feature of NMR that distinguishes it from all other forms of spectroscopy is that interactions involving many sites of known identity can be probed simultaneously. The sites comprise NMR observable nuclei (^{1}H, ^{15}N, ^{13}C) whose resonance

assignments in the major species are readily obtained using modern triple resonance NMR spectroscopy.[15] Using global fitting procedures in which all the RD data at the observed sites are fitted simultaneously, it is possible to dissect kinetic pathways, although in general this is limited in complexity to three-site exchange models.[3–5,16]

The most commonly employed nucleus for RD experiments is the ^{15}N of the backbone amide groups. Yet, the structural information provided by ^{15}N chemical shifts alone is generally quite limited unless reference ^{15}N chemical shifts are already available for the various states being studied. More recent developments have extended RD measurements to $^{1}H_N$, $^{13}C\alpha$, $^{1}H\alpha$, $^{13}C\beta$, and $^{13}C'$ backbone atoms, as well as to side chain methyl groups.[17–21] This opens the way to obtain highly reliable backbone ϕ/ψ torsion angle restraints for minor states derived from complete backbone chemical shifts using programs such as TALOS+.[22] Further, recent advances have shown that it is possible to calculate structures of small proteins (less than ~120 residues) from a near complete set of backbone chemical shifts: the latter are used to first select peptide fragments from a database; the fragments are subsequently assembled into 3D models, which are scored based on their agreement with the chemical shift data as well as other energy terms.[23–25] Such procedures provide a potential avenue for obtaining full 3D structural information on sparsely populated states.[26] Caution, however, needs to be exercised when the minor species involves a partially unfolded or disordered state since the techniques employed to generated 3D models based on chemical shifts rely on databases derived from folded proteins.

Under suitable circumstances, it is also possible to use RD measurements to obtain bond vector orientation information on minor states.[27–30] Two NMR observables are available, residual dipolar couplings (RDC) and residual chemical shift anisotropy (RCSA). Both involve the use of weakly aligned media (such as dilute solutions of bicelles and filamentous phages) to reintroduce anisotropic magnetic interactions that are otherwise averaged to zero in isotropic solution.[31] Because these effects are small, highly accurate RD measurements are required and the experiments are extremely demanding. A proof of principle has been provided in a model system involving a protein–ligand interaction where the RDCs and RCSAs can be measured in the unliganded and fully liganded states.[29]

RD spectroscopy is primarily a kinetic technique that yields rate constants in systems undergoing chemical exchange between species characterized by different chemical shifts. The structural information in the form of chemical shifts, and in certain cases bond vector orientational information from RDCs and RCSAs, is in a sense a by-product of the data analysis. The structural information derived from RD experiments is necessarily critically dependent on the kinetic model used to fit the RD curves. As in any kinetic experiment, the application of Occam's Razor is required: that is the simplest kinetic scheme required to fit the data is considered to be correct unless proven otherwise. Given that data from a large number of sites are measured, one might conclude that if the RD data can be fit globally, for example, to a two-site exchange model, then a three-site exchange process is unlikely. Nevertheless, the interpretation of RD-derived structural parameters in terms of atomic structures must be applied with caution since the values of these structural parameters will obviously be dependent on the kinetic model used to fit the RD data. Thus, for example, consider the case of a system involving exchange between a major species and two sparsely populated states where the exchange rate between the two minor states is faster than the time scale of the RD experiment. Under these conditions, the RD data would be accounted for by a two-site exchange model[16] and the structural parameters obtained for the minor species would be given by the weighted average of the individual structural parameters of the two sparsely populated states. Unless there was additional information to indicate that indeed the minor species detected by the RD experiments was a mixture of states, it is clear that the structural interpretation of the minor state would in this instance be in error.

Some examples of systems probed by RD measurements

RD measurements have been used to probe a range of important biological phenomena. Only a few examples will be highlighted here.

A system that is perhaps ideal for the application of RD spectroscopy involves the study of folding intermediates under conditions where such an intermediate(s), in equilibrium with the folded and unfolded states, is populated.[5] Examples of such studies include the Fyn SH3 domain[32] and the FF domain of HYPA/FBP11.[26] In the case of Fyn SH3, it was shown that mutation of a conserved residue (Gly48) destabilized the protein and increased the folding rate. RD measurements were carried out on two such mutants at several magnetic fields and temperatures, and the data were fit globally to a three-site exchange model.[32] The rate constants for interconversion between the folded, unfolded and intermediate states were obtained as well as the backbone ^{15}N chemical shifts of the intermediate state. The latter were then used to calculate the degree of unfolding in any given residue from the value of $(\delta F - \delta I)/(\delta F - \delta U)$, where δF, δI, and δU are the chemical shifts of the folded, intermediate and unfolded states, respectively. A more

comprehensive RD study of the FF domain was carried out under conditions where the folded state was in equilibrium with an intermediate state, and the population of the unfolded state was so low that it could be neglected.[26] In this study, RD data were used to obtain essentially complete backbone shifts and N—H RDCs on the intermediate. With this information at hand, CS-Rosetta[24] was used to propose a 3D model for the intermediate. The native FF domain comprises a four-helix bundle, as does the intermediate, and the overall topologies of the two states are essentially the same. However, the length of the third helix is increased in the intermediate whereas that of the fourth helix is reduced, and the overall flexibility of the intermediate is enhanced relative to the folded state.

Another area that is particular suited to RD measurements lies in probing the relationship between molecular motions and the rate-limiting step in catalysis.[33–35] Two examples involving interdomain motions in phosphoryl transfer enzymes, adenylate cyclase[36,37] and enzyme $II^{Mannitol}$,[38] have been examined by RD spectroscopy. Adenylate kinase undergoes a transition from an open state in the absence of substrate to a closed state in the presence of substrate, involving large-scale correlated motions within the hinge region connecting the lid and AMP-binding domains to the core domain of the enzyme. This conformational transition involves lid closure of the active site. Under turnover conditions, the rate constant for lid closure measured from RD spectroscopy is fast, while that for lid opening is slow. Further, for both thermophilic and mesophilic enzymes the rate constants for lid opening are found to be equal, within experimental error, to the corresponding values of k_{cat} obtained from steady-state kinetic measurements. Thus, in the case of adenylate kinase the rate-limiting step in catalysis is not the phosphoryl transfer event but product release.[36,37] Enzyme II^{Mtl} of the mannitol branch of the bacterial phosphotransferase system (PTS) comprises two cytoplasmic domains and a transmembrane domain connected by flexible linkers, 20–30 residues in length. The phosphoryl group is transferred from the A domain to the B domain and subsequently onto the incoming sugar bound to the cytoplasmic side of the C domain. The A and B domains can be expressed separately and their chemical shifts are known both free and bound to one another. With this information in hand, it is possible to directly obtain the proportion of open dissociated and closed associated states in a IIA^{Mtl}-IIB^{Mtl} single chain construct. The rates of association and dissociation obtained from RD measurements are approximately equal ($\sim 2 \times 10^4$ s^{-1}) and ~40-fold faster than the rate of phosphoryl transfer (~ 500 s^{-1}) derived from ^{31}P lineshape analysis during turnover. Thus in the case of IIA^{Mtl}-IIB^{Mtl}, the rate limiting step is the phosphoryl transfer reaction and on average ~80 association/dissociation events take place for every successful phosphoryl transfer.[38]

RD spectroscopy has also been used to characterize stable intermediates in the catalytic cycle of dihydrofolate reductase (DHFR).[39–41] The key finding is that each intermediate samples a sparsely populated state that resembles the major species of either the preceding or subsequent step in the catalytic cycle. Further, the rates measured from RD spectroscopy match the rates obtained from transient kinetic measurements. Thus, for example, the dissociation rate for $NADP^+$ release from the ternary DHFR-$NADP^+$-tetrahydrofolate complex matches the rate at which the binary DHFR-tetrahydrofolate complex samples a minor state analogous to the ternary DHFR-$NADP^+$-tetrahydrofolate complex; likewise, the rate of product release from the ternary DHFR-NADPH-tetrahydrofolate complex matches the rate at which this ternary complex samples a minor state resembling the DHFR-NADPH binary complex. These data suggest that pre-existing conformational transitions involving sparsely populated states play a key role in catalysis by "funneling catalytically competent conformations along a kinetically preferred path."[40]

Another area where RD spectroscopy has been fruitfully applied lies in the problem of coupled folding and binding of intrinsically disordered peptides.[42,43] The phosphorylated kinase inducible activation domain (pKID) of the transcription factor CREB is an intrinsically disordered polypeptide that folds into a helical structure, comprising two α-helices, upon binding to its target, the KIX domain of the transcriptional coactivator CPB. RD experiments demonstrate unambiguously that folding of pKID is induced upon binding and proceeds via a partially folded intermediate.[43]

Paramagnetic relaxation enhancement (PRE)

The PRE, in contrast to RD spectroscopy, yields structural information directly but cannot be used to obtain kinetic information (e.g., rate constants). The PRE arises from magnetic dipolar interactions between the unpaired electrons of a paramagnetic center and a nucleus, such as a proton.[44,45] This effect results in an increase in the relaxation rate of nuclear magnetization that is proportional to the $\langle r^{-6} \rangle$ average distance between the electron and the nucleus of interest. Because the magnetic moment of an unpaired electron is large, the PRE effect is very large and can extend to distances as large as ~35 Å, in contrast to the ^1H—^1H nuclear Overhauser effect (NOE), which extends out to only ~6 Å. In the absence of an intrinsic paramagnetic center, a paramagnetic label has to be introduced via an engineered surface cysteine.[46] For the purpose of PRE measurements, the most suitable labels are ones that have an unpaired electron with an

isotropic g-tensor.[8] The most common labels are nitroxide spin-labels and metal ions such as Mn^{2+} and Gd^{3+} chelated, for example, to EDTA,[47] with functional groups that permit the facile formation of a covalent S—S (or C—S) bond to the engineered surface cysteine. The PRE is obtained from the difference in relaxation rates between the paramagnetic and control diamagnetic states. PREs can be measured on both longitudinal (Γ_1) and transverse (Γ_2) relaxation rates, but the latter affords the most reliable way to make use of the PRE.[8,9] First the magnitude of the ^{1}H-Γ_2 rate is much larger than the ^{1}H-Γ_1 rate, making the ^{1}H-Γ_2 PRE a much more sensitive probe; second the ^{1}H-Γ_2 rate is much less susceptible to internal motions and cross-relaxation than the ^{1}H-Γ_1 rate.

The underlying theory of the PRE for static systems dates back to the late 1950s[44,45] and the PRE has long been used in the study of paramagnetic metalloproteins.[48–50] The potential of the PRE for structure determination of single proteins was first demonstrated in the mid-1980s[51,52] but then largely neglected until about 10 years ago with the advent of straightforward biochemical methods for introducing paramagnetic labels at specific sites in proteins.[53–55] Moreover, the quantitative use of the PRE for structure determination was thwarted until very recently when an appropriate theoretical framework and computational methods were developed to take into account the large conformational space sampled by a paramagnetic label attached to the protein via a linker with multiple rotatable bonds.[56] By representing the paramagnetic label by an ensemble of states and taking care to calculate PRE order parameters from the coordinates during the course of structure refinement, it is now possible to directly refine against the PRE relaxation rates and obtain accurate structures where agreement between the model and the experimental data is quantitatively assessed by a Q-factor (analogous to a crystallographic R-factor).[8,56]

The key to using the PRE to detect transient low-population species lies in rapid exchange phenomena whereby the transverse PRE observed on a major species is modulated by the presence of the minor species (Fig. 1).[57] In a two-site exchange system comprising two species A and B that interconvert on a time scale that is fast on the PRE time scale (defined as $k_{ex} \gg |\Gamma_2^B - \Gamma_2^A|$ where k_{ex} is the sum of the forward and backward rate constants, and Γ_2^B and Γ_2^A are the transverse PRE rates for species B and A, respectively), the observed PRE measured on either resonance will be the population weighted average of the PRE rates for the two species.

Consider a system where a particular paramagnetic center-proton distance is 30 Å for species A and 8 Å for species B [Fig. 1(A)]. The corresponding Γ_2 PRE rates (for a system ~30 kDa in size) will have values of ~2 s^{-1} and ~5600 s^{-1}, respectively. If species A and B are populated at 99% and 1%, respectively, species B will be effectively invisible in the NMR spectrum. In the fast exchange limit, however, the observed PRE, Γ_2^{obs}, measured on the resonance of the major, NMR-visible, species A will be ~50 s^{-1}, much larger than that expected for species A alone [Fig. 1(B)]. Therefore, providing distances between the paramagnetic center and the protons of interest are significantly shorter in the minor species than the major one, and the interconversion rate between the two species is fast, the PRE profiles observed on the major species will reveal the footprint of the minor species. The PRE profiles can be analyzed quantitatively to derive structural information if the PRE profile for the major species is either known or can be calculated from a known structure. As the exchange rate decreases, the influence of the minor species on the observed PRE profile for the major species will be reduced until in the slow exchange limit the PRE profile for the major species will be unaffected by the presence of the minor species [Fig. 1(B)]. Thus, the use of the PRE to detect and characterize sparsely populated states is limited to rapidly exchanging systems, typically with lifetimes less than 250−500 μs. In the following sections we will discuss examples pertaining to specific protein-DNA interactions, protein-protein association and large-scale interdomain conformational transitions.

PRE detection of sliding and intermolecular translocation in specific protein-DNA interactions

Initially, we had developed the relevant theory and refinement tools for the PRE as a method of structure determination to provide long-range (up to 35 Å) distance information[56] as a complement to the short-range distance information (<6 Å) afforded by the ^{1}H-^{1}H NOE, which provides the mainstay of NMR structure determination.[58,59] We had shown for the specific SRY/DNA complex that direct refinement against intermolecular PRE data is readily feasible and yields increased coordinate accuracy as judged by cross-validation against RDCs.[56] We had subsequently extended these PRE studies to a related complex involving the homologous nonspecific DNA binding protein HMGB-1A.[60] The structures of the SRY/DNA and HMG-1A/DNA complexes are very similar but whereas SRY binds to a specific 8 base pair site on the DNA, HMGB-1A binds nonspecifically to any 8 base pair DNA segment. This is reflected in the intermolecular PRE profiles: the PRE profiles observed with labels placed at the two ends of the DNA are distinct for the SRY/DNA complex but very similar for the HMGB-1A/DNA complex, diagnostic of multiple site binding in two possible orientations [related by a 180° rotation; Fig. 2(A)]. Since

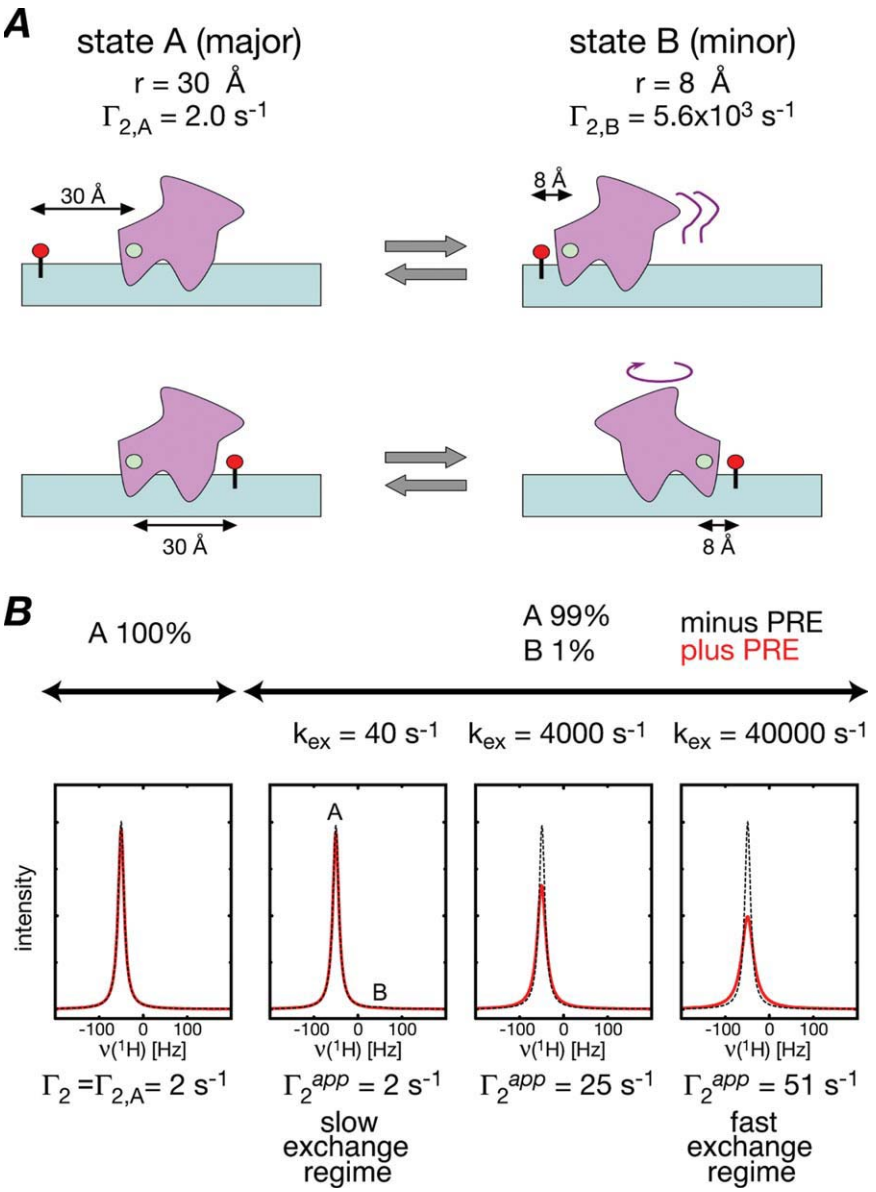

Figure 1. Basis for the detection of short-lived, sparsely populated species by PRE. (*A*) Schematic of a two-site exchange process in which the major (99%) and minor (1%) species have paramagnetic center-^{1}H distances of 30 and 8 Å, respectively. (*B*) Effect of exchange rate on the NMR line-shape of the resonance of the major species A in the presence (red) and absence (black) of the PRE. The resonances of the major species A and NMR-invisible minor species B are located at −50 and +50 Hz, respectively of the carrier position. Reproduced from Ref. 57.

exchange of HMGB-1A between the different possible DNA binding sites is fast on the chemical shift time scale, an ensemble averaged Γ_2 rate (given by the weighted average of the Γ_2 rates for all the individual states) is observed for each paramagnetic center-proton vector from which it is then possible to compute the occupancies at all possible DNA binding sites [Fig. 2(B)]. The highest populations of HMGB-1A are found in the central region of the DNA duplex and the populations in the two possible orientations are approximately equal.[60]

The finding that the intermolecular PRE was capable of detecting both sliding of a protein along the DNA as well as intermolecular translocation of a protein from one DNA molecule to another in a specific protein-DNA complex was entirely fortuitous. We had been interested in studying the structure of a ternary complex involving the HoxD9 homeodomain, HMGB-1A, and DNA. Despite numerous reports in the literature that HoxD9 and HMGB-1A interacted with one another both in the absence and presence of DNA, we were unable to detect any NMR evidence for such an interaction (Iwahara, J. and Clore, G.M., unpublished data). However, since the presence of HMGB-1A was reported to enhance transcriptional activation by HoxD9 we speculated that the effect of HoxD9 bound to DNA was to modulate the distribution of nonspecifically bound HMGB-1A on the DNA, and hence alter the extent of DNA bending induced by HMGB-1A. We never addressed this issue in the end because

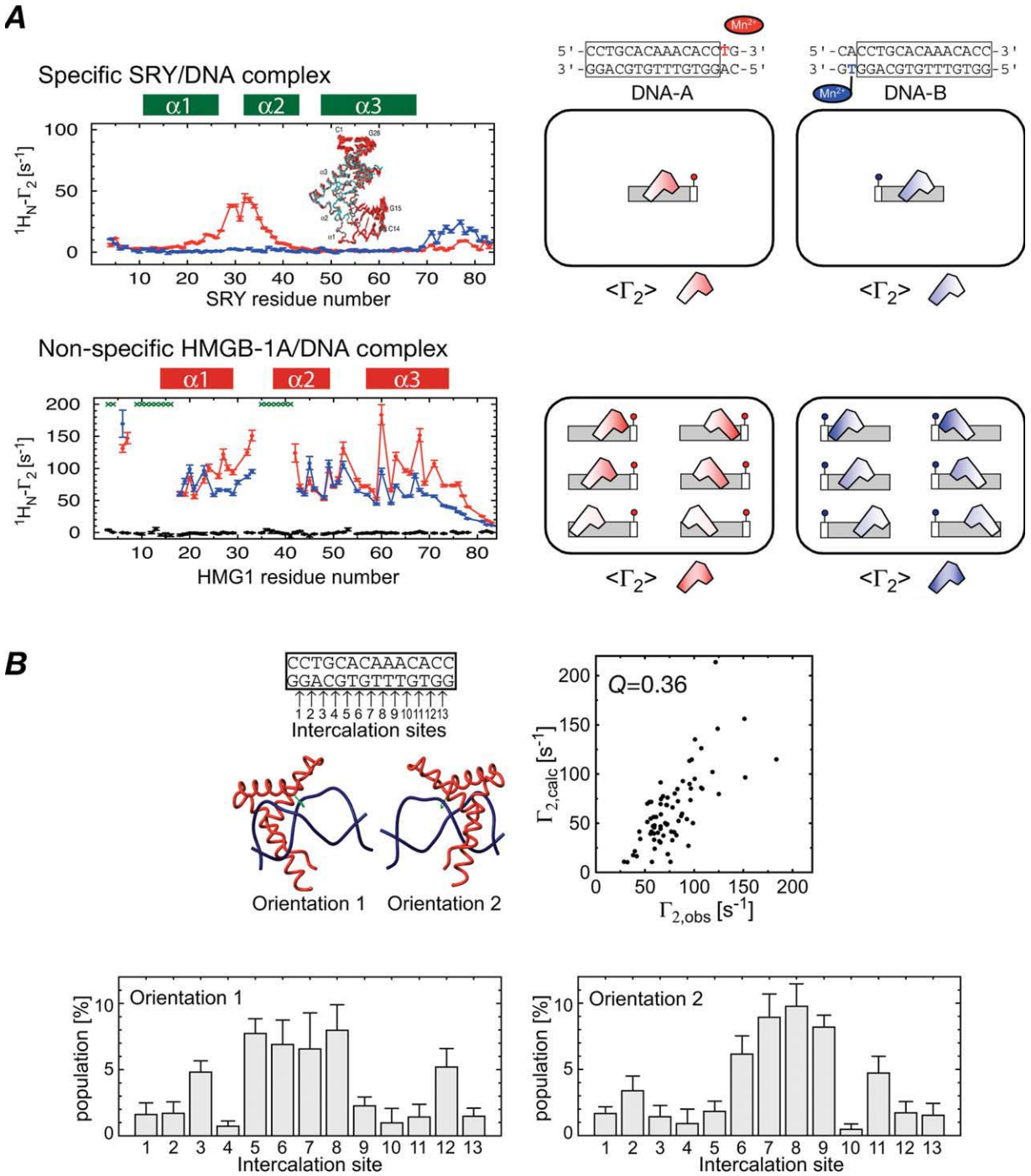

Figure 2. Characterization of nonspecific DNA binding by PRE. (*A*) Comparison of intermolecular PREs observed for the specific SRY/DNA complex (top) and the nonspecific HMGB-1A/DNA complex (bottom) using two DNA duplexes with the paramagnetic dT-EDTA-Mn^{2+} label located at opposite ends of the DNA. The states giving rise to PREs in the two complexes are depicted as cartoons in the right-hand panels. The inset in the top left-panel is the structure of the SRY/DNA complex determined from NOE, RDC, and intermolecular PRE data.[56] (*B*) Semi-quantitative analysis of site occupancy of HMGB-1A on the DNA. There are 13 possible binding sites and HMGB-1A can bind in two orientations related by a 180° rotation (top left). The agreement between calculated and observed PRE rates is shown in the top right-hand panel and the calculated occupancies at the binding sites are shown in the two bottom panels. Reproduced from Ref. 60.

control experiments on the specific HoxD9/DNA binary complex revealed a totally unexpected finding that opened the door for using the PRE to detect and probe transient sparsely populated states.[57]

Intermolecular PRE data recorded at low ionic strength (20 m*M* NaCl) for the specific HoxD9/DNA complex using four different paramagnetic sites on the DNA [Fig. 3(A)] were fully consistent with

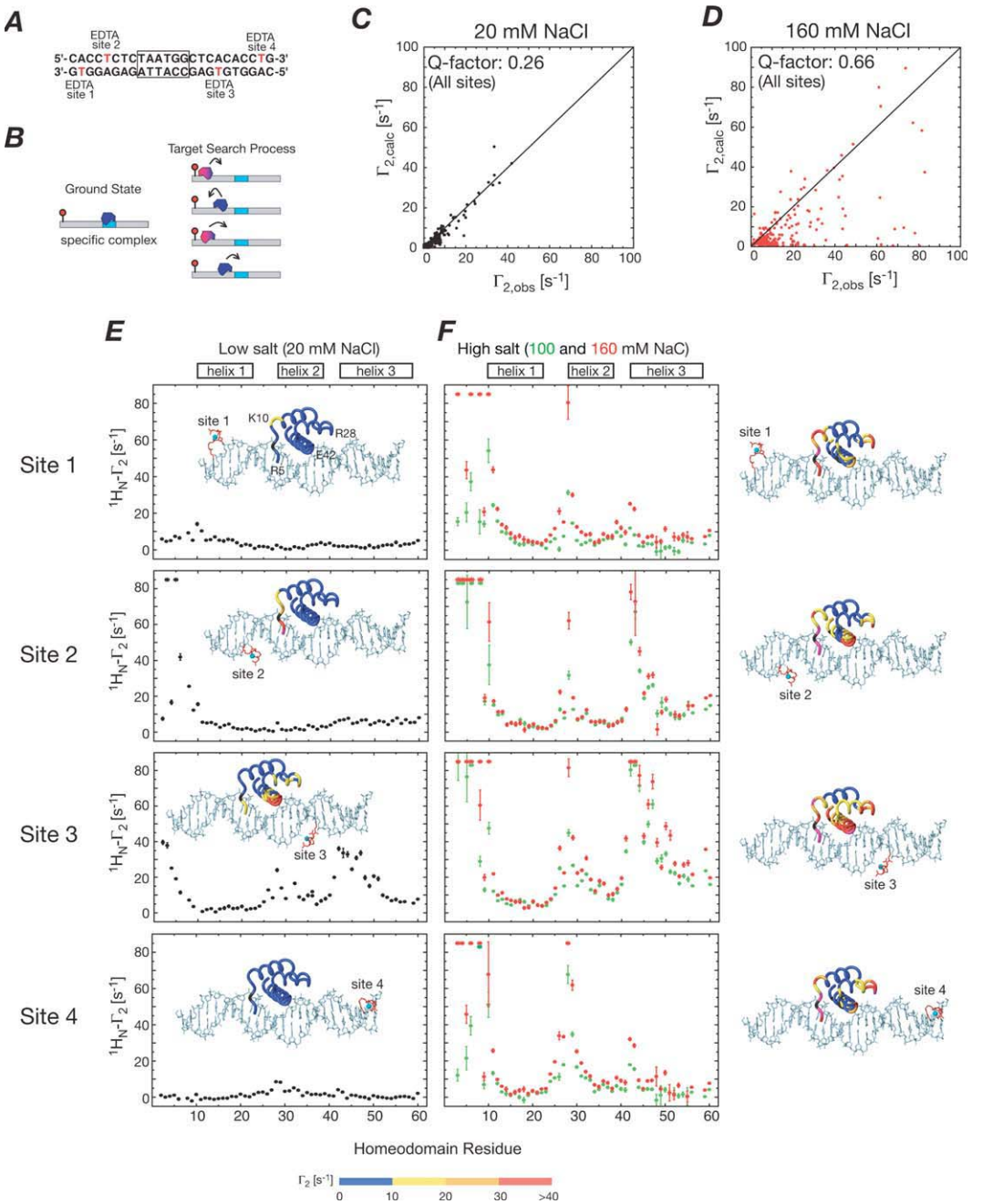

Figure 3. Intermolecular PREs observed for the specific HoxD9/DNA complex in the slow (20 m*M* NaCl) and fast (>100 m*M* NaCl) PRE exchange regimes. (*A*) DNA duplexes showing the location of the four dT-EDTA-Mn^{2+} paramagnetic labels (one per sample) with the specific site boxed. (*B*) Cartoon comparing the ground state specific complex with nonspecific complexes formed during the target search process. (*C*) and (*D*) Comparison of observed and calculated PREs at low (20 m*M* NaCl) and high (160 m*M* NaCl) salt, respectively, corresponding to the slow and fast PRE exchange regimes. At low salt, the agreement with the structure of the specific complex is excellent, whereas minimal agreement is seen at high salt. This is due to intramolecular sliding and fast direct intermolecular translocation from one DNA molecule to another without the protein dissociating into free solution. (The rate constant for dissociation of specifically bound HoxD9 into free solution at 150 m*M* NaCl is $< 0.01\ s^{-1}$). (*E*) and (*F*) Intermolecular PRE profiles observed for the four paramagnetic sites at low and high salt, respectively. PREs mapped onto the structure of the specific complex are also shown for low (insets) and high (to the right of the PRE profiles) salt conditions with the color scale depicting the ranges of PRE rates. Reproduced from Ref. 57.

the structure of the complex [*Q*-factor = 0.26; Figs. 3(C,E)]. However, at higher salt concentrations (100 and 160 m*M* NaCl) completely unexpected PRE profiles were observed [Figs. 3(D,F)] despite the fact that the equilibrium dissociation constant for HoxD9 at 150 m*M* salt is ~1.5 n*M*, the dissociation rate constant is less than $0.01\ s^{-1}$, and there are no detectable structural changes in the complex at higher

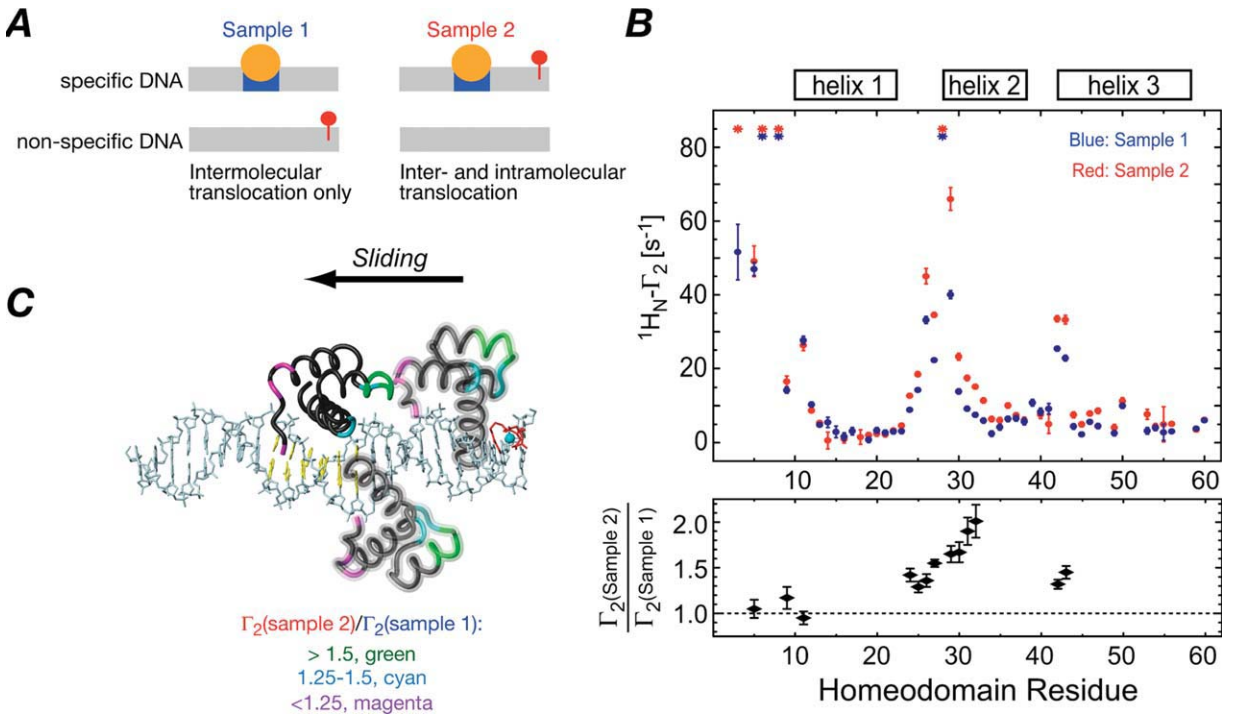

Figure 4. Dissection of intramolecular sliding and direct intermolecular translocation processes for the HoxD9/DNA complex. (*A*) In sample 1, comprising an equal mixture of specific and nonspecific DNA with the nonspecific DNA bearing the paramagnetic label, intermolecular PREs can only arise from intermolecular translocation. In sample 2, the specific DNA bears the paramagnetic label and the nonspecific DNA is unlabeled (i.e., diamagnetic) so that both inter- and intramolecular translocation can give rise to PRE effects. (*B*) PRE profiles observed for samples 1 (blue) and 2 (red) (top panel). The ratios of the PRE rates observed for samples 2 and 1 are shown in the bottom panel. Schematic diagram of HoxD9 sliding along the DNA with HoxD9 color coded according to the Γ_2(sample 2)/Γ_2(sample 1) ratios. Reproduced from Ref. 57.

salt since the chemical shifts remain unchanged and the RDCs at low and high salt are highly correlated (correlation coefficient $r = 0.99$). At both 100 and 160 m*M* NaCl, similar large magnitude, intermolecular PRE profiles were observed for symmetrically placed labels at opposite ends of the DNA duplex with very poor agreement between observed and calculated PREs [*Q*-factor = 0.66; Figs. 3(D,F)]. Thus, we surmised that the intermolecular PRE profiles at high salt reflect the existence of short-lived, sparsely populated states [Fig. 3(B)] involving intramolecular one-dimensional sliding of HoxD9 along the DNA,[61] as well as intermolecular translocation from one DNA molecule to another without going through the intermediary of free protein.[62–64] Since the ratio of specific to nonspecific equilibrium dissociation constants is about 200, the population of these transient states is estimated to be ~0.5%.

The contributions from sliding and intermolecular translocation can be ascertained from two complementary experiments [Fig. 4(A)] in which HoxD9 is added to an equal mixture of specific and nonspecific DNA duplexes, with the paramagnetic label located on either the nonspecific duplex or the specific duplex.[57] In the first instance, intermolecular PREs can only arise from rapid intermolecular translocation in which HoxD9 is transferred from the specific DNA duplex to the nonspecific DNA duplex and back again; in the second both sliding and intermolecular translocation can give rise to intermolecular PREs. The PRE profiles for the two samples are very similar, but the intensities of the PREs observed on resonances of the DNA recognition helix (residues 23–33) as well as residues 41–42 are 30–100% larger in the second sample than the first, whereas the magnitude of the PREs for the N-terminal arm are the same for the two samples [Fig. 4(B)]. These experiments indicate that (a) intermolecular translocation is a major contributor to the observed intermolecular PREs and (b) the larger PRE effects observed for residues 23–33 and 41–42 in the second sample are due to sliding along the DNA and arise from bias since the orientation of HoxD9 bound to the specific site is favored as the protein slides along the DNA: in this configuration the recognition helix can come close to the paramagnetic label while the N-terminal arm is always far away [Fig. 4(C)]. The N-terminal tail can only come into close proximity of the paramagnetic label following an intermolecular translocation event accompanied by a 180° change in binding orientation on the DNA duplex containing the specific site.

PRE detection and characterization of transient encounter complexes in protein-protein association

Encounter complexes in protein-protein association represent the two-dimensional equivalent of one-dimensional diffusion (sliding) in specific protein-DNA recognition. Thus, two proteins first associate nonspecifically to form a pre-equilibrium encounter complex that subsequently relaxes via two-dimensional diffusion on the surface of the proteins to form the stereospecific complex.[65] The kinetic significance of encounter complexes is evidenced by the observation that both site-directed mutagenesis[66,67] and Brownian dynamics simulations[68–70] have shown that perturbations in charge distributions outside the direct interaction surfaces can modulate the rate of protein-protein association.

The first direct demonstration and characterization of encounter complexes by PRE measurements was carried out on complexes of the bacterial PTS, a signal transduction pathway in which multiple phosphoryl transfer steps between weak, sequential binary protein-protein complexes is coupled to transport and phosphorylation of an incoming sugar.[71] The first complex of the pathway is between enzyme I (EI) and the histidine phosphocarrier protein HPr. The complex between the N-terminal domain of EI (EIN) and HPr solved by NMR from NOE and RDC data is fully consistent with the formation of a pentacoordinate phosphoryl transition state intermediate without requiring any significant structural perturbations.[72] Intramolecular PREs for HPr, measured on a complex comprising EIN at natural isotopic abundance and U-[^{15}N]-HPr paramagnetically labeled at three separate sites (individually), are fully consistent with the structure of HPr [Q-factor = 0.18, Fig. 5(A)]. Many of the features of the intermolecular PREs from paramagnetically labeled HPr to ^{15}N-labeled EIN are also consistent with the structure of the complex; however, quite a number of sizeable intermolecular PREs are observed involving residues far away from the paramagnetic labels indicative of the existence of sparsely populated transient states [Figs. 5(B,C)].[71]

Knowing the structure of the specific complex, it was then possible using rigid body simulated annealing to calculate an ensemble of states to represent the encounter complex that fully account for the observed PRE profiles [Fig. 5(D)]. It was found that the population of the encounter complex ensemble was approximately 10% and between 10 and 20 structures were required to represent the ensemble. The distribution of the encounter complex ensemble was correlated with the electrostatic distribution on the surface of the proteins[71] and the population of the encounter complex could be modulated by ionic strength indicating a substantial electrostatic contribution.[73]

By monitoring the intermolecular PRE rates on ^{15}N-labeled EIN as a function of the concentration of paramagnetically labeled HPr, two distinct types of encounter complexes were identified (Fig. 6).[74] The first is in direct equilibrium with and occluded by the stereospecific complex, probably involves rigid body rotations and small translations at or near the active site, and likely is most important for initially guiding HPr into the productive conformation when the active site is empty. The second can coexist with the specific complex to form a ternary complex ensemble and involves two major patches on the surface of the protein, one of which is quite close to the active site and may serve as a docking site for a second molecule of HPr to bind while the active site is occupied and involved in phosphoryl transfer. This type of encounter complex may accelerate specific association by properly orienting the second HPr molecule via electrostatic steering, regardless of the occupancy of the EIN active site, and may be important for efficiently reloading the EIN active site when demand for sugar transport is high by increasing the effective local concentration of HPr in the vicinity of the active site (Fig. 6).[74]

Transient encounter complexes are not unique to the EIN-HPr complex. Similar encounter complexes for other complexes of the PTS,[71] as well as several electron transfer complexes[75–79] were subsequently detected by PRE measurements.

PRE analysis of transient ultra-weak self-association

Transient self-association of proteins is relevant to assembly and maturation processes. This can be investigated by intermolecular PRE measurements in a manner similar to that employed for hetero-encounter complexes described in the previous section. Thus, measurements are carried out on an equal mixture of isotopically labeled (e.g., ^{15}N/^{2}H) protein and paramagnetically labeled protein at natural isotopic abundance. Using this approach ultra-weak self-association of HPr was detected with a $K_D \geq 15$ mM corresponding to a population of $\sim$1% under the experimental conditions employed.[80]

Similar PRE studies have been carried out on the HIV-1 protease precursor.[81] Mature HIV-1 protease is an obligate dimer with residues from both subunits contributing to the active site. The protease precursor, however, bearing as little as an additional 4 residues N-terminal to the mature protease is monomeric, yet undergoes maturation via a first order process, implying intramolecular cleavage of a transient precursor dimer. In the mature protease the N- and C-termini are part of an intersubunit β-sheet that is distal from the active site. PRE measurements on two precursors with different N-terminal extensions showed that highly transient, sparsely populated (3–5%) dimeric encounter complexes are indeed formed using the

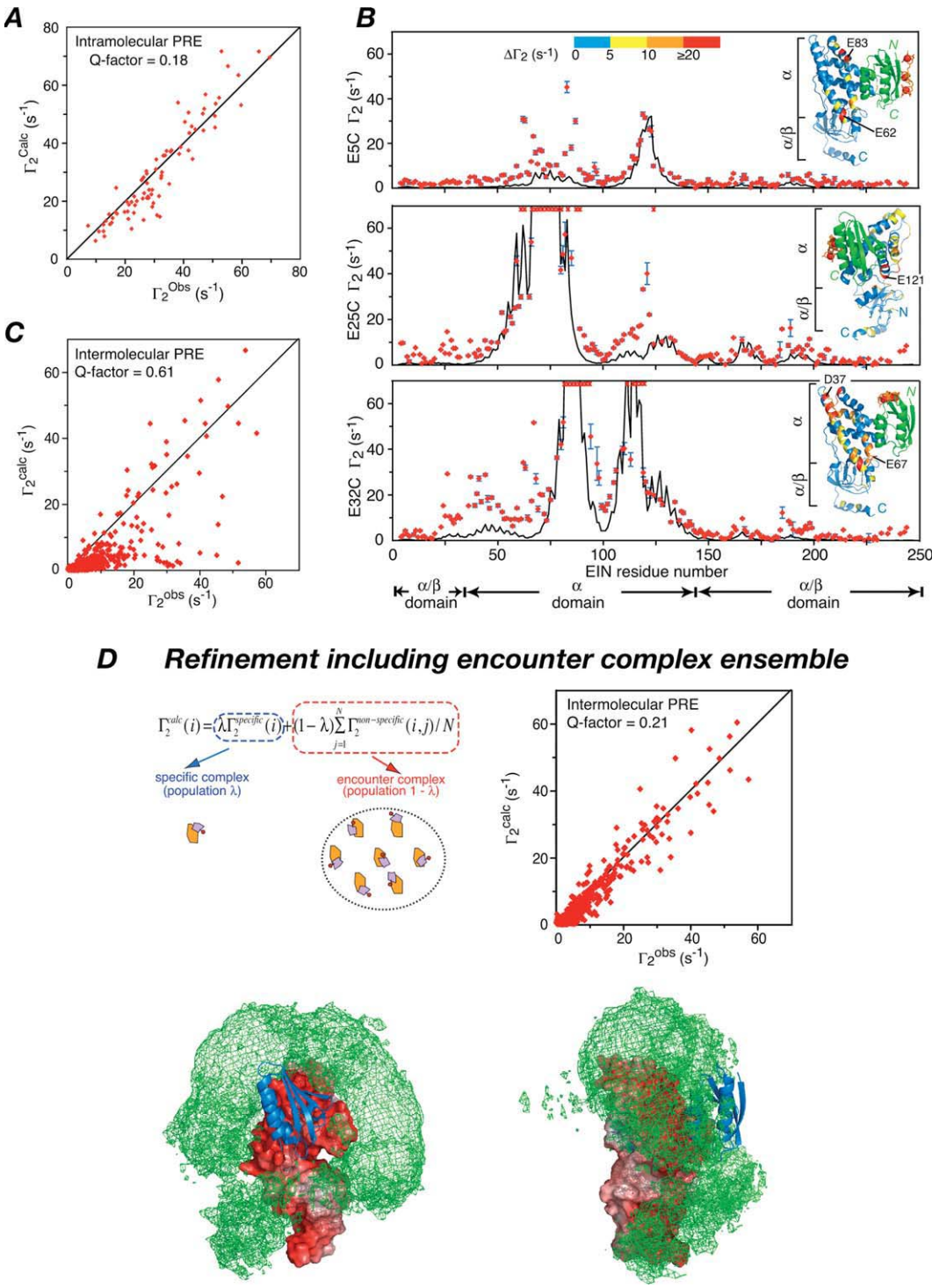

Figure 5. PRE detection of encounter complexes in protein-protein association illustrated by the EIN/HPr complex. HPr was paramagnetically labeled at three sites (E5C, E25C, and E32C) one at a time with EDTA-Mn^{2+}. (*A*) Intramolecular PRE data recorded on HPr in the EIN/HPr complex (with HPr ^{15}N-labeled and EIN at natural isotopic abundance) display excellent agreement between observed and calculated PRE rates. (*B*) The experimental intermolecular PRE profiles observed on ^{15}N-labeled EIN (red circles) show many features attributable to the specific complex with the calculated PREs for the specific complex shown in black, but regions with large discrepancies are apparent where the observed intermolecular PREs are much larger than predicted from the structure of the complex and involve residues located far away from the interaction surfaces. (*C*) Agreement between observed intermolecular PRE rates and those calculated from the structure of the EIN/HPr complex show poor quantitative agreement. (*D*) Refinement against the PRE data including the encounter complex ensemble using Xplor-NIH.[92] The observed PRE rate for residue *i* is given as a population weighted average of the PRE rates for residue *i* in the specific complex and the encounter complex ensemble (top left). The optimal ensemble size for the encounter complex is 10−20, and, with a population of 10% for the encounter complex ensemble, excellent agreement between observed and calculated PRE rates is obtained (top right). Two views of a reweighted atomic probability distribution map (green mesh plotted at a threshold of 20% maximum[93]) showing the distribution of HPr on the surface of EIN in the encounter complex ensemble. (The probability map is calculated from 100 independent calculations each comprising an ensemble size of 20 for the encounter complex ensemble.) The molecular surface of EIN is color coded by electrostatic potential (±8 kT) and the location of HPr in the specific complex is shown as a blue ribbon. Reproduced from Ref. 71.

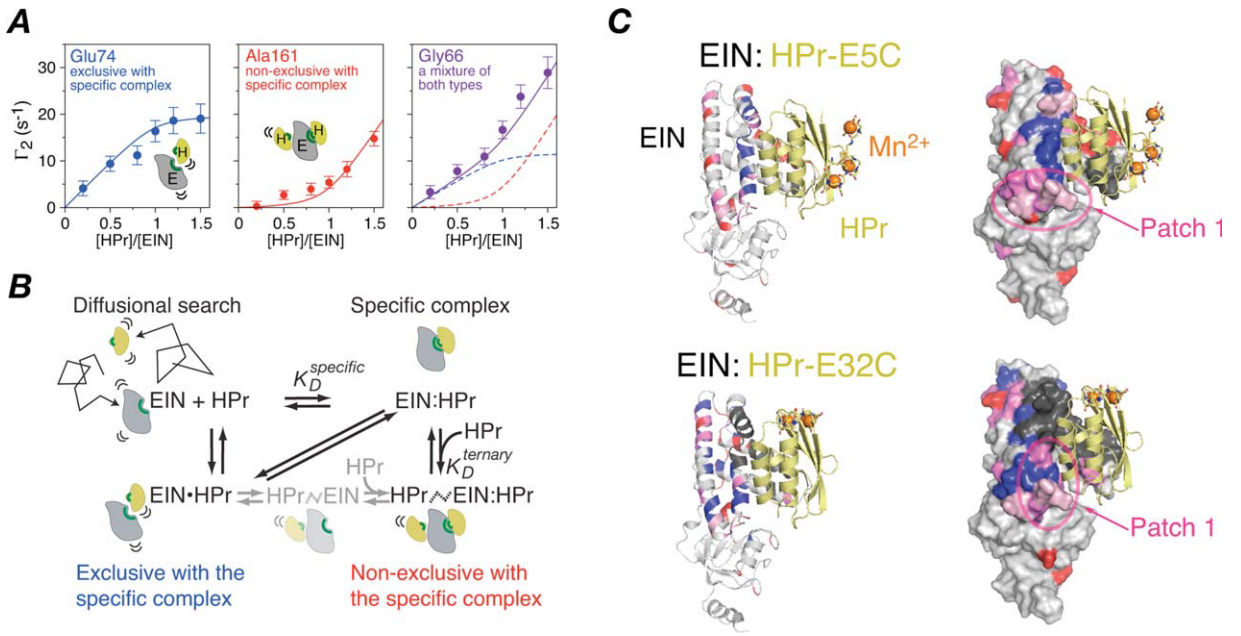

Figure 6. Mechanistic details of the EIN-HPr association pathway revealed by intermolecular PRE titration measurements. (*A*) Examples of PRE titration curves obtained upon adding paramagnetically labeled HPr-E5C(EDTA-Mn^{2+}) to ^{15}N-labeled EIN. Three classes of PRE titration behavior are observed: class I scales linearly with the concentration of the specific EIN/HPr complex (blue line; e.g., Glu74 of EIN); class II scales linearly with the concentration of free HPr (red line; e.g., Ala161 of EIN); and class III behaves as a mixture of classes I and II and fits to a scaled sum (purple line; e.g., Gly66 of EIN) of the specific EIN/HPr (blue dashed line) and free HPr (red dashed line) concentrations. The insets are cartoons of class I and II encounter complexes of HPr (yellow) on the surface of EIN (gray) with the interaction surfaces on the two proteins colored in green. (*B*) Equilibrium binding model for the EIN/HPr association pathway deduced from the PRE data. Upon collision EIN and HPr form two types of encounter complexes: the first is in competitive equilibrium with the specific complex and therefore exclusive with the specific complex, while the second forms simultaneously with the specific complex to form a ternary complex. (*C*) Intermolecular PREs at the final titration point mapped onto the surface of EIN. EIN is displayed as a ribbon model in the left panels and as a molecular surface in the right panels, color coded according to the predominant (>80% contribution from classes I or II) type of intermolecular nonspecific PRE observed at a particular residue. Blue, red and purple indicate encounter complex PREs of classes I, II, and III, respectively; pink are encounter complex PREs that have Γ_2 rates that are too large (>65 s^{-1}) to measure accurately; and dark gray indicates specific PREs with Γ_2 rates > 25 s^{-1}. The purple ellipse labeled Patch 1 highlights a region on the surface of EIN where class II PREs cluster in reasonably close proximity to the active site. A second cluster of class II PREs is located on the opposite face of EIN, far from the active site. HPr is shown in the specific configuration (yellow ribbon) in all panels with the EDTA-Mn^{2+} paramagnetic label displayed as a three-conformer ensemble with the Mn^{2+} atoms shown as orange spheres. Reproduced from Ref. 74.

same interface as that in the mature dimer. In contrast to the mature dimer, however, a wide range of subunit orientations is sampled and the occupancy of the mature dimer conformation constitutes an extremely small faction of the self-associated species, thereby accounting for the very low enzymatic activity of the precursor. Further, it could be shown that the N-terminal extension present in the precursor makes both transient intrasubunit and intersubunit contacts with the substrate binding site, and is therefore available for autocleavage upon sampling of the correct dimer orientation.

PRE characterization of transient large-scale domain reorientations

Many proteins undergo conformational changes upon ligand binding. In some instances these involve large, rigid body domain reorientations. The question arises as to whether the ligand-bound state can be sampled in the absence of ligand. A classic example is that of the two-domain maltose binding protein, MBP.[82–86] In the absence of ligand, the structure is in an open state. Upon binding ligand the two domains undergo a 35° reorientation closing like a fly trap and burying the ligand. The conformational change involves a hinge-bending motion within the short linker region connecting the two domains. RDC and small angle X-ray scattering data on both the "apo" and "holo" states of MBP are fully consistent with the corresponding crystal structures.[84,85,87] However, both these observables are linear population averages of the species present in solution and therefore insensitive to the presence of minor species.

For both apo and holo MBP the intradomain PRE data are fully consistent with the crystal structures of the two domains. The interdomain PRE

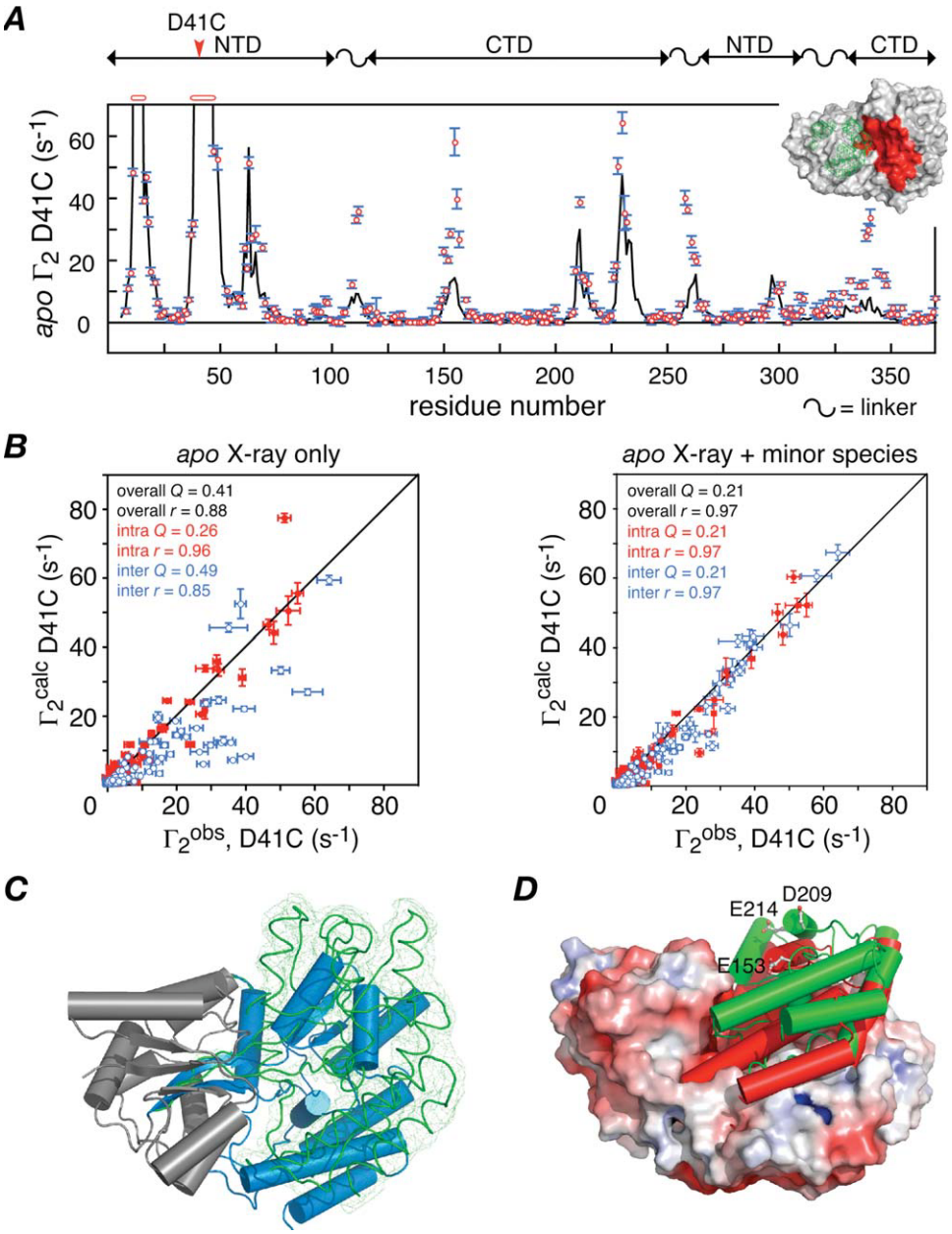

Figure 7. PRE detection of a partially closed state of apo MBP. (*A*) PRE profiles observed for apo MBP with the spin-label located at position D41C on the N-terminal domain. The experimental PREs are shown as red circles and the PRE profile calculated from the crystal structure of apo MBP are displayed as a solid line. The inset shows a molecular surface of apo MBP with the conformational space sample by the oxygen atom of the nitroxide spin label represented by a green mesh and residues with PRE discrepancies ($\Gamma_2^{obs} - \Gamma_2^{calc} > 10\ s^{-1}$) colored in red. (*B*) Comparison of observed versus calculated intradomain (red) and interdomain (blue) PREs obtained with the crystal structure of apo MBP (left panel) and upon inclusion of a minor species at an occupancy of 5% (right panel). (*C*) Superposition of the major open apo state (i.e., the crystal structure) with the partially closed apo state calculated from the PRE data. The N-terminal domains of the two states (gray cylinders) are superimposed; the C-terminal domain is displayed as blue cylinders for the open state and as a green smoothed backbone trace with a reweighted atomic probability map for the partially closed state. (*D*) Structural comparison of the open apo, partially closed apo and holo states with the N-terminal domain of all three states superimposed. The open apo state is shown as a molecular surface color-coded according to electrostatic potential. The C-terminal domain of the partially closed apo and closed holo states are shown as green and red cylinders, respectively. Reproduced from Ref. 87.

data for holo MBP are also fully consistent with the holo crystal structure. For apo MBP, however, the interdomain PRE profiles, while qualitatively similar, are significantly larger in magnitude than those predicted from the apo crystal structure [Figs. 7(A,B)]. Although the PRE data can be accounted for by a single alternate conformation, this conformation is not compatible with the RDC

data. Thus, apo MBP must exist as a mixture of a major species corresponding to the apo crystal structure and a sparsely populated transient state.[87] Since $^{1}H_N$-$R_{1\rho}$ RD is not observed, the upper limit for the time scale of interconversion between these states is estimated to be less than ~20 μs, with a lower limit of ~20 ns corresponding to the rotational correlation time as ^{15}N-{^{1}H} heteronuclear NOE data provide no evidence for large scale picosecond to nanosecond motions within the linker region.

Given the known crystal structure of the major apo species, it is possible to calculate an $<r^{-6}>$ average structure for the minor species by conjoined rigid body/torsion angle simulated annealing refinement in which the PRE data originating from two paramagnetically labeled sites are fitted simultaneously to a two-member ensemble of major open and minor species, with the major species held fixed in the apo crystal structure conformation.[87] The PRE data are fully accounted for by a single partially closed minor species with an occupancy of ~5% [Fig. 7(B)]. The transition between the major and minor species also involves a ~35° hinge-body rotation [Fig. 7(C)], but the minor species is not the same as the holo state, differing by a ~20° rotation and 6 Å translation of the C-terminal domain relative to the N-terminal domain [Fig. 7(D)].

The minor apo species comprises a partially closed state that leaves the sugar-binding pocket on the C-terminal domain exposed. In the absence of ligand, the holo conformation is energetically highly unfavorable[86] owing to the close proximity of negative charges on the two domains that are not neutralized by bridging hydrogen bonds with the substrate.[83] These unfavorable electrostatic interactions are mitigated in the partially closed minor apo species by translation of the C-terminal domain out of the sugar-binding pocket, thereby exposing several negatively charged residues and increasing the interdomain distance between negatively charged residues on the two domains [Fig. 7(D)].[87] Since the conformational transition in the apo state does not involve the holo conformation, the conformational change from the apo to the holo state upon ligand binding can be regarded as an example of induced fit. However, the existence of a partially closed apo state that is closer to the holo conformation than the open apo state can be viewed as an example of conformational selection that may facilitate and prime sugar binding.

Differential transverse relaxation measurements

In systems that involve exchange processes between an NMR-visible state and an NMR-invisible high molecular weight species (i.e., a "dark" state), enhancements in transverse (R_2) relaxation rates can arise from a lifetime broadening effect as a result of direct incorporation of the NMR-visible species into the NMR-invisible one. As an example, the ^{15}N R_2 rates for free α-synuclein are enhanced by 2–5 s^{-1} upon addition of lipid vesicles, reflecting the pseudo-first order association rate constant k_{on}^{app} for the binding of α-synuclein to the lipid vesicles.[88,89] The same phenomenon has been observed for amyloid β (Aβ) under pseudo-equilibrium conditions where the sample is stably partitioned between monomeric Aβ peptide and large molecular weight oligomers or protofibrils.[10]

In the case of Aβ, a pseudo-equilibrium is established in 1–2 weeks after which the partitioning of Aβ between monomer and oligomer remains stable for up to 6–8 weeks. The ratio of monomer to oligomer is dependent upon the total concentration of Aβ in the sample. As the total concentration of Aβ is increased, the R_2 rate enhancements (ΔR_2, measured as the difference in R_2 rates between samples at high and low concentrations of Aβ) for the resonances of monomeric Aβ become larger. The ΔR_2 values are independent of magnetic field strength (600 and 900 MHz) and nucleus (^{1}H and ^{15}N), and show minimal variation along the polypeptide chain (Fig. 7). From the data it can be ascertained that k_{on}^{app} has values of ~1.1 and ~3 s^{-1} at total Aβ concentrations of 150 and 300 μ*M*, respectively.

The dissociation rate constant, k_{off}, as well as the R_2 relaxation rates for the NMR-invisible "dark" state can be obtained by analysis of saturation profiles in which the attenuation of the integrated intensity of the amide proton envelope upon application of an off-resonance radiofrequency field (RF) is monitored as a function of offset from the carrier frequency (in this case at the water resonance).[10] From these data a value of ~73 s^{-1} is obtained for k_{off}. In addition, the "dark" state is characterized phenomenologically by two different R_2 relaxation rates of ~40,000 s^{-1} and ~300 s^{-1} with weights of 40 and 60%, respectively. The latter explains the small variations in ΔR_2 rates observed for the monomer, with slightly smaller ΔR_2 rates for the first nine N-terminal residues (which are disordered in Aβ fibrils) and residues 24–29 (which form a turn between two β-strands in Aβ fibrils) on account of their higher mobility in the oligomer-bound state, and maximal ΔR_2 rates equal to k_{on}^{app} for regions in intimate contact with the oligomer such as the central hydrophobic region [Fig. 8(A)].

The fraction of peptide in the "dark" state that undergoes exchange with free monomer, which is readily calculated from the known concentration of free monomer and the values of k_{on}^{app} and k_{off}, is actually very low (3–4%), illustrating how sensitive this technique is to sparsely populated states. It is also worth noting that the exchange processes between "NMR-visible" and "NMR-invisible" protofibril-like, oligomeric species being observed in these experiments is six orders of magnitude faster than the rates of molecular recycling within fully formed amyloid fibrils observed by NMR and mass spectrometry H/D exchange experiments.[90,91]

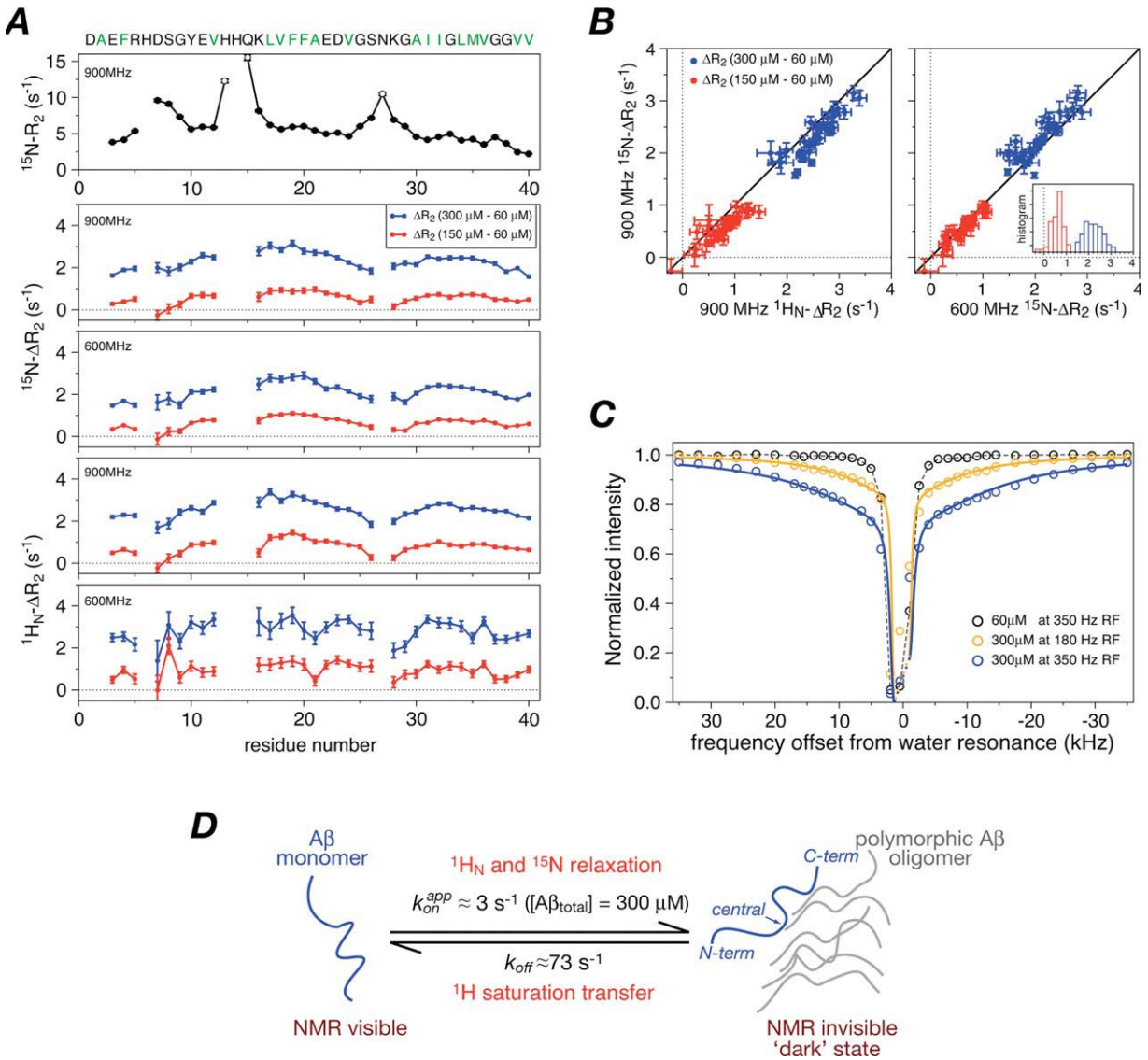

Figure 8. Kinetics of amyloid β (Aβ) monomer-to-oligomer exchange derived from differential relaxation measurements. (*A*) ^{1}H and ^{15}N transverse relaxation rates measured on equilibrated samples of Aβ(1−40). The top panel shows the ^{15}N-R_2 rates for the 60 μ*M* Aβ sample as a function of residue; the other panels display the difference in R_2 rates between the 300 (blue) or 150 (red) μ*M* Aβ samples and the 60 μ*M* Aβ sample for ^{1}H and ^{15}N at 600 and 900 MHz. The variation of ΔR_2 as a function of residue is minimal, and the maximal ΔR_2 rates provide the value for the pseudo-first order association rates for the conversion of monomer to oligomer. (*B*) Correlation plots showing that ΔR_2 is independent of nucleus and magnetic field. (*C*) ^{1}H transfer of saturation profiles for the ^{1}H$_N$-envelope of monomeric Aβ as a function of offset of a weak off-resonance radio frequency (RF) field. Black circles, 60 μ*M* Aβ and 350 Hz RF field; orange and blue circles, 300 μ*M* Aβ at 180 and 350 RF fields, respectively. The solid curves represent the best-fits to the data using the McConnell equations[94] for a dipolar coupled two-spin, two-site exchange model yielding an off-rate of ∼73 s^{-1} for dissociation of an Aβ unit from the oligomer into free solution. (*D*) Two-site exchange kinetic scheme for the interconversion rates between monomeric and oligomeric forms of Aβ. The oligomer is characterized by large (∼40,000 s^{-1}) and small (∼300 s^{-1}) R_2 rates with populations of ∼0.4 and ∼0.6, respectively. This reflects regions of Aβ that are either tightly bound to the oligomer (e.g. central hydrophobic region) or that retain significant mobility in the oligomer (e.g., N-terminus), respectively. The fraction of oligomer that undergoes exchange with free monomer is 3−4%. Reproduced from Ref. 10.

Concluding Remarks

We have presented a brief overview of several recently developed NMR approaches for studying short-lived, sparsely populated states with occupancies as low as 0.5%. RD experiments are dependent upon chemical shift differences between the major and minor species resulting in exchange line broadening for processes occurring on time scales ranging from ∼50 μs to ∼10 ms. Global fitting of RD data affords kinetic models and associated rate constants with structural information in the form of chemical shifts and, in suitable cases, bond vector orientations as a bonus of the analysis. PRE experiments provide direct structural information and are suitable for

probing events with time scales less than ~250−500 μs. The PRE is not dependent on chemical shift differences between the states, but does require the existence of paramagnetic center-nucleus distances that are significantly shorter in the minor species than the major one. Minor states in which all the paramagnetic center-^{1}H distances are longer in the minor species than in the major species are invisible to the PRE method. This is because the observed PREs in the fast exchange regime are a population weighted average of the PREs for the states present in solution. Because the PRE is related to the $<r^{-6}>$ separation between the paramagnetic center and the monitored nucleus, the magnitudes of the effects at short distances are very large and, consequently, the PRE profiles observed on the resonances of the major species can reveal the footprint of the minor species. Finally, differential transverse relaxation measurements can probe exchange events between NMR-visible and high-molecular weight NMR-invisible species in the millisecond time regime by lifetime broadening effects in the absence of chemical shift differences.

The ability of these various NMR experiments to detect and analyze short-lived, sparsely populated states lies in the fact that many sites and interactions are probed simultaneously, and therefore interpretation of the data is not reliant on a single or very limited number of interactions. Further, the availability of a very large number of NMR observables, in the form of chemical shifts, bond vector orientations or paramagnetic center-proton distances, provides the key for obtaining detailed structural information on sparsely populated states.

In conclusion, the development of new NMR experiments in the form of RD spectroscopy and PRE has opened the way for detecting, visualizing, and characterizing transient sparsely populated states, and has shed fundamental new insights into a wide range of biological and biophysical processes.

Acknowledgments

I thank A. Szabo for useful discussions and J. Iwahara, C.D. Schwieters, and C. Tang for fruitful collaborations.

References

1. Palmer AG III, Kroenke CD, Loria JP (2001) Nuclear magnetic resonance methods for quantifying microsecond-to-millisecond motions in biological macromolecules. Methods Enzymol 339:204–238.
2. Baldwin AJ, Kay LE (2009) NMR spectroscopy brings invisible protein states into focus. Nat Chem Biol 5: 808–814.
3. Korzhnev DM, Kay LE (2008) Probing invisible, low-populated states of protein molecules by relaxation dispersion NMR spectroscopy: an application to protein folding. Acc Chem Res 41:442–451.
4. Mittermaier AK, Kay LE (2009) Observing biological dynamics at atomic resolution using NMR. Trends Biochem Sci 34:601–611.
5. Neudecker P, Lundstrom P, Kay LE (2009) Relaxation dispersion NMR spectroscopy as a tool for detailed studies of protein folding. Biophys J 96:2045–2054.
6. Loria JP, Berlow RB, Watt ED (2008) Characterization of enzyme motions by solution NMR relaxation dispersion. Acc Chem Res 41:214–221.
7. Clore GM (2008) Visualizing lowly-populated regions of the free energy landscape of macromolecular complexes by paramagnetic relaxation enhancement. Mol Biosyst 4:1058–1069.
8. Clore GM, Iwahara J (2009) Theory, practice, and applications of paramagnetic relaxation enhancement for the characterization of transient low-population states of biological macromolecules and their complexes. Chem Rev 109:4108–4139.
9. Clore GM, Tang C, Iwahara J (2007) Elucidating transient macromolecular interactions using paramagnetic relaxation enhancement. Curr Opin Struct Biol 17:603–616.
10. Fawzi NL, Ying J, Torchia DA, Clore GM (2010) Kinetics of amyloid β monomer-to-oligomer exchange by NMR relaxation. J Am Chem Soc 132:9948–9951.
11. Palmer AG III, Grey MJ, Wang C (2005) Solution NMR spin relaxation methods for characterizing chemical exchange in high-molecular-weight systems. Methods Enzymol 394:430–465.
12. Palmer AG III, Massi F (2006) Characterization of the dynamics of biomacromolecules using rotating-frame spin relaxation NMR spectroscopy. Chem Rev 106: 1700–1719.
13. Carr HY, Purcell EM (1954) Effects of diffusion on free precession in nuclear magnetic resonance experiments. Phys Rev 94:630–638.
14. Meiboom S, Gill D (1958) Modified spin-echo method for measuring nuclear relaxation times. Rev Sci Instrum 29:688–691.
15. Cavanagh J, Fairbrother WJ, Palmer AG III, Rance M, Skelton NJ (2007) Protein NMR Spectroscopy: Principles and Practice, 2nd ed. New York: Academic Press.
16. Trott O, Palmer AG III (2004) Theoretical study of $R_{1\rho}$ rotating-frame and R_2 free-precession relaxation in the presence of *n*-site chemical exchange. J Magn Reson 170:104–112.
17. Ishima R, Torchia DA (2003) Extending the range of amide proton relaxation dispersion experiments in proteins using a constant-time relaxation-compensated CPMG approach. J Biomol NMR 25:243–248.
18. Hansen DF, Vallurupalli P, Lundstrom P, Neudecker P, Kay LE (2008) Probing chemical shifts of invisible states of proteins with relaxation dispersion NMR spectroscopy: how well can we do? J Am Chem Soc 130:2667–2675.
19. Lundstrom P, Vallurupalli P, Religa TL, Dahlquist FW, Kay LE (2007) A single-quantum methyl 13C-relaxation dispersion experiment with improved sensitivity. J Biomol NMR 38:79–88.
20. Lundstrom P, Hansen DF, Vallurupalli P, Kay LE (2009) Accurate measurement of α proton chemical shifts of excited protein states by relaxation dispersion NMR spectroscopy. J Am Chem Soc 131:1915–1926.
21. Lundstrom P, Lin H, Kay LE (2009) Measuring ^{13}Cβ chemical shifts of invisible excited states in proteins by relaxation dispersion NMR spectroscopy. J Biomol NMR 44:139–155.
22. Shen Y, Delaglio F, Cornilescu G, Bax A (2009) TALOS+: a hybrid method for predicting protein backbone torsion angles from NMR chemical shifts. J Biomol NMR 44:213–223.

23. Cavalli A, Salvatella X, Dobson CM, Vendruscolo M (2007) Protein structure determination from NMR chemical shifts. Proc Natl Acad Sci U S A 104: 9615–9620.
24. Shen Y, Lange O, Delaglio F, Rossi P, Aramini JM, Liu G, Eletsky A, Wu Y, Singarapu KK, Lemak A, Ignatchenko A, Arrowsmith CH, Szyperski T, Montelione GT, Baker D, Bax A (2008) Consistent blind protein structure generation from NMR chemical shift data. Proc Natl Acad Sci U S A 105:4685–4690.
25. Shen Y, Vernon R, Baker D, Bax A (2009) *De novo* protein structure generation from incomplete chemical shift assignments. J Biomol NMR 43:63–78.
26. Korzhnev DM, Religa TL, Banachewicz W, Fersht AR, Kay LE (2010) A transient and low-populated protein-folding intermediate at atomic resolution. Science 329: 1312–1316.
27. Hansen DF, Vallurupalli P, Kay LE (2008) Using relaxation dispersion NMR spectroscopy to determine structures of excited, invisible protein states. J Biomol NMR 41:113–120.
28. Vallurupalli P, Hansen DF, Stollar E, Meirovitch E, Kay LE (2007) Measurement of bond vector orientations in invisible excited states of proteins. Proc Natl Acad Sci U S A 104:18473–18477.
29. Vallurupalli P, Hansen DF, Kay LE (2008) Structures of invisible, excited protein states by relaxation dispersion NMR spectroscopy. Proc Natl Acad Sci U S A 105: 11766–11771.
30. Vallurupalli P, Hansen DF, Kay LE (2008) Probing structure in invisible protein states with anisotropic NMR chemical shifts. J Am Chem Soc 130:2734–2735.
31. Bax A, Grishaev A (2005) Weak alignment NMR: a hawk-eyed view of biomolecular structure. Curr Opin Struct Biol 15:563–570.
32. Korzhnev DM, Salvatella X, Vendruscolo M, Di Nardo AA, Davidson AR, Dobson CM, Kay LE (2004) Low-populated folding intermediates of Fyn SH3 characterized by relaxation dispersion NMR. Nature 430:586–590.
33. Villali J, Kern D (2010) Choreographing an enzyme's dance. Curr Opin Chem Biol 14:636–643.
34. Henzler-Wildman K, Kern D (2007) Dynamic personalities of proteins. Nature 450:964–972.
35. Kern D, Eisenmesser EZ, Wolf-Watz M (2005) Enzyme dynamics during catalysis measured by NMR spectroscopy. Methods Enzymol 394:507–524.
36. Wolf-Watz M, Thai V, Henzler-Wildman K, Hadjipavlou G, Eisenmesser EZ, Kern D (2004) Linkage between dynamics and catalysis in a thermophilic-mesophilic enzyme pair. Nat Struct Mol Biol 11:945–949.
37. Henzler-Wildman KA, Thai V, Lei M, Ott M, Wolf-Watz M, Fenn T, Pozharski E, Wilson MA, Petsko GA, Karplus M, Hubner CG, Kern D (2007) Intrinsic motions along an enzymatic reaction trajectory. Nature 450:838–844.
38. Suh JY, Iwahara J, Clore GM (2007) Intramolecular domain-domain association/dissociation and phosphoryl transfer in the mannitol transporter of Escherichia coli are not coupled. Proc Natl Acad Sci U S A 104:3153–3158.
39. Boehr DD, Dyson HJ, Wright PE (2008) Conformational relaxation following hydride transfer plays a limiting role in dihydrofolate reductase catalysis. Biochemistry 47:9227–9233.
40. Boehr DD, McElheny D, Dyson HJ, Wright PE (2006) The dynamic energy landscape of dihydrofolate reductase catalysis. Science 313:1638–1642.
41. Boehr DD, McElheny D, Dyson HJ, Wright PE (2010) Millisecond timescale fluctuations in dihydrofolate reductase are exquisitely sensitive to the bound ligands. Proc Natl Acad Sci U S A 107:1373–1378.
42. Wright PE, Dyson HJ (2009) Linking folding and binding. Curr Opin Struct Biol 19:31–38.
43. Sugase K, Dyson HJ, Wright PE (2007) Mechanism of coupled folding and binding of an intrinsically disordered protein. Nature 447:1021–1025.
44. Solomon I (1955) Relaxation processes in a system of two spins. Phys Rev 99:559–565.
45. Bloembergen N, Morgan LO (1961) Proton relaxation times in paramagnetic solutions: effects of electron spin relaxation. J Chem Phys 34:842–850.
46. Kosen PA (1989) Spin labeling of proteins. Methods Enzymol 177:86–121.
47. Iwahara J, Anderson DE, Murphy EC, Clore GM (2003) EDTA-derivatized deoxythymidine as a tool for rapid determination of protein binding polarity to DNA by intermolecular paramagnetic relaxation enhancement. J Am Chem Soc 125:6634–6635.
48. Cheng H, Markley JL (1995) NMR spectroscopic studies of paramagnetic proteins: iron-sulfur proteins. Annu Rev Biophys Biomol Struct 24:209–237.
49. Bertini I, Luchinat C, Piccioli M (2001) Paramagnetic probes in metalloproteins. Methods Enzymol 339: 314–340.
50. Ubbink M, Worrall JA, Canters GW, Groenen EJ, Huber M (2002) Paramagnetic resonance of biological metal centers. Annu Rev Biophys Biomol Struct 31:393–422.
51. Schmidt PG, Kuntz ID (1984) Distance measurements in spin-labeled lysozyme. Biochemistry 23:4261–4266.
52. Kosen PA, Scheek RM, Naderi H, Basus VJ, Manogaran S, Schmidt PG, Oppenheimer NJ, Kuntz ID (1986) Two-dimensional ^{1}H-NMR of three spin-labeled derivatives of bovine pancreatic trypsin inhibitor. Biochemistry 25:2356–2364.
53. Battiste JL, Wagner G (2000) Utilization of site-directed spin labeling and high-resolution heteronuclear nuclear magnetic resonance for global fold determination of large proteins with limited nuclear overhauser effect data. Biochemistry 39:5355–5365.
54. Gaponenko V, Howarth JW, Columbus L, Gasmi-Seabrook G, Yuan J, Hubbell WL, Rosevear PR (2000) Protein global fold determination using site-directed spin and isotope labeling. Protein Sci 9:302–309.
55. Donaldson LW, Skrynnikov NR, Choy WY, Muhandiram DR, Sarkar B, Forman-Kay JD, Kay LE (2001) Structural characterization of proteins with an attached ATCUN motif by paramagnetic relaxation enhancement NMR spectroscopy. J Am Chem Soc 123: 9843–9847.
56. Iwahara J, Schwieters CD, Clore GM (2004) Ensemble approach for NMR structure refinement against ^{1}H paramagnetic relaxation enhancement data arising from a flexible paramagnetic group attached to a macromolecule. J Am Chem Soc 126:5879–5896.
57. Iwahara J, Clore GM (2006) Detecting transient intermediates in macromolecular binding by paramagnetic NMR. Nature 440:1227–1230.
58. Wüthrich K (1986) NMR of proteins and nucleic acids. Hoboken, New Jersey: Wiley.
59. Clore GM, Gronenborn AM (1991) Structures of larger proteins in solution: three- and four-dimensional heteronuclear NMR spectroscopy. Science 252:1390–1399.
60. Iwahara J, Schwieters CD, Clore GM (2004) Characterization of nonspecific protein-DNA interactions by ^{1}H paramagnetic relaxation enhancement. J Am Chem Soc 126:12800–12808.
61. Berg OG, Winter RB, von Hippel PH (1981) Diffusion-driven mechanisms of protein translocation on nucleic acids. 1. Models and theory. Biochemistry 20: 6929–6948.

62. Iwahara J, Clore GM (2006) Direct observation of enhanced translocation of a homeodomain between DNA cognate sites by NMR exchange spectroscopy. J Am Chem Soc 128:404–405.
63. Iwahara J, Zweckstetter M, Clore GM (2006) NMR structural and kinetic characterization of a homeodomain diffusing and hopping on nonspecific DNA. Proc Natl Acad Sci U S A 103:15062–15067.
64. Doucleff M, Clore GM (2008) Global jumping and domain-specific intersegment transfer between DNA cognate sites of the multidomain transcription factor Oct-1. Proc Natl Acad Sci U S A 105:13871–13876.
65. Kim YC, Tang C, Clore GM, Hummer G (2008) Replica exchange simulations of transient encounter complexes in protein-protein association. Proc Natl Acad Sci U S A 105:12855–12860.
66. Schreiber G, Fersht AR (1996) Rapid, electrostatically assisted association of proteins. Nat Struct Biol 3: 427–431.
67. Selzer T, Albeck S, Schreiber G (2000) Rational design of faster associating and tighter binding protein complexes. Nat Struct Biol 7:537–541.
68. Northrup SH, Boles JO, Reynolds JC (1988) Brownian dynamics of cytochrome c and cytochrome c peroxidase association. Science 241:67–70.
69. Spaar A, Dammer C, Gabdoulline RR, Wade RC, Helms V (2006) Diffusional encounter of barnase and barstar. Biophys J 90:1913–1924.
70. Gabdoulline RR, Wade RC (2002) Biomolecular diffusional association. Curr Opin Struct Biol 12:204–213.
71. Tang C, Iwahara J, Clore GM (2006) Visualization of transient encounter complexes in protein-protein association. Nature 444:383–386.
72. Garrett DS, Seok YJ, Peterkofsky A, Gronenborn AM, Clore GM (1999) Solution structure of the 40,000 M_r phosphoryl transfer complex between the N-terminal domain of enzyme I and HPr. Nat Struct Biol 6: 166–173.
73. Suh JY, Tang C, Clore GM (2007) Role of electrostatic interactions in transient encounter complexes in protein-protein association investigated by paramagnetic relaxation enhancement. J Am Chem Soc 129:12954–12955.
74. Fawzi NL, Doucleff M, Suh JY, Clore GM (2010) Mechanistic details of a protein-protein association pathway revealed by paramagnetic relaxation enhancement titration measurements. Proc Natl Acad Sci U S A 107: 1379–1384.
75. Volkov AN, Worrall JA, Holtzmann E, Ubbink M (2006) Solution structure and dynamics of the complex between cytochrome c and cytochrome c peroxidase determined by paramagnetic NMR. Proc Natl Acad Sci U S A 103:18945–18950.
76. Volkov AN, Bashir Q, Worrall JA, Ubbink M (2009) Binding hot spot in the weak protein complex of physiological redox partners yeast cytochrome c and cytochrome c peroxidase. J Mol Biol 385:1003–1013.
77. Ubbink M (2009) The courtship of proteins: understanding the encounter complex. FEBS Lett 583: 1060–1066.
78. Volkov AN, Bashir Q, Worrall JA, Ullmann GM, Ubbink M (2010) Shifting the equilibrium between the encounter state and the specific form of a protein complex by interfacial point mutations. J Am Chem Soc 132:11487–11495.
79. Bashir Q, Volkov AN, Ullmann GM, Ubbink M (2010) Visualization of the encounter ensemble of the transient electron transfer complex of cytochrome c and cytochrome c peroxidase. J Am Chem Soc 132:241–247.
80. Tang C, Ghirlando R, Clore GM (2008) Visualization of transient ultra-weak protein self-association in solution using paramagnetic relaxation enhancement. J Am Chem Soc 130:4048–4056.
81. Tang C, Louis JM, Aniana A, Suh JY, Clore GM (2008) Visualizing transient events in amino-terminal autoprocessing of HIV-1 protease. Nature 455:693–696.
82. Quiocho FA, Spurlino JC, Rodseth LE (1997) Extensive features of tight oligosaccharide binding revealed in high-resolution structures of the maltodextrin transport/chemosensory receptor. Structure 5:997–1015.
83. Sharff AJ, Rodseth LE, Spurlino JC, Quiocho FA (1992) Crystallographic evidence of a large ligand-induced hinge-twist motion between the two domains of the maltodextrin binding protein involved in active transport and chemotaxis. Biochemistry 31:10657–10663.
84. Skrynnikov NR, Goto NK, Yang D, Choy WY, Tolman JR, Mueller GA, Kay LE (2000) Orienting domains in proteins using dipolar couplings measured by liquid-state NMR: differences in solution and crystal forms of maltodextrin binding protein loaded with beta-cyclodextrin. J Mol Biol 295:1265–1273.
85. Evenas J, Tugarinov V, Skrynnikov NR, Goto NK, Muhandiram R, Kay LE (2001) Ligand-induced structural changes to maltodextrin-binding protein as studied by solution NMR spectroscopy. J Mol Biol 309:961–974.
86. Millet O, Hudson RP, Kay LE (2003) The energetic cost of domain reorientation in maltose-binding protein as studied by NMR and fluorescence spectroscopy. Proc Natl Acad Sci U S A 100:12700–12705.
87. Tang C, Schwieters CD, Clore GM (2007) Open-to-closed transition in apo maltose-binding protein observed by paramagnetic NMR. Nature 449:1078–1082.
88. Bodner CR, Dobson CM, Bax A (2009) Multiple tight phospholipid-binding modes of α-synuclein revealed by solution NMR spectroscopy. J Mol Biol 390:775–790.
89. Bodner CR, Maltsev AS, Dobson CM, Bax A (2010) Differential phospholipid binding of α-synuclein variants implicated in Parkinson's disease revealed by solution NMR spectroscopy. Biochemistry 49:862–871.
90. Carulla N, Caddy GL, Hall DR, Zurdo J, Gairi M, Feliz M, Giralt E, Robinson CV, Dobson CM (2005) Molecular recycling within amyloid fibrils. Nature 436:554–558.
91. Carulla N, Zhou M, Giralt E, Robinson CV, Dobson CM (2010) Structure and intermolecular dynamics of aggregates populated during amyloid fibril formation studied by hydrogen/deuterium exchange. Acc Chem Res 43: 1072–1079.
92. Schwieters CD, Kuszewski J, Clore GM (2006) Using Xplor-NIH for NMR molecular structure determination. Progr Nucl Magn Reson Spectrosc 48:47–62.
93. Schwieters CD, Clore GM (2002) Reweighted atomic densities to represent ensembles of NMR structures. J Biomol NMR 23:221–225.
94. McConnell HM (1958) Reaction rates by nuclear magnetic resonance. J Chem Phys 28:430–431.